



Supplementary Materials for

Pectin homogalacturonan nanofilament expansion drives morphogenesis in plant epidermal cells

Kalina T. Haas^{*}, Raymond Wightman, Elliot M. Meyerowitz, and Alexis Peaucelle^{*}

^{*}These authors contributed equally to this work.

correspondence to: Alexis.Peaucelle@inrae.fr or Kalina.Haas@inrae.fr

This PDF file includes:

Materials and Methods
Figs. S1 to S11
Captions for Movies S1 to S7
Captions for Audio S1 to S2
References (43, 44)
MDAR Reproducibility Checklist

Other Supplementary Materials for this manuscript includes the following:

Movies S1 to S7 (.avi)
Audio S1 to S2 (.wav)

Materials and Methods

Plant growth conditions

Plants were grown on solid media as described in (2), in constant light. Ethanol induction was performed as described in (2). The PME5-overexpressing (OE) lines and PME13-overexpressing lines were described previously in (2, 29, 30). The effect of the overexpression was tested through the changes in the HG methylation level quantified with immunolabeling.

Time-lapse imaging of cotyledons

Time-lapse cotyledon imaging was performed with a Keyence VHX-5000 (KEYENCE (UK) LIMITED Milton Keynes, U.K.) digital microscope using coaxial light with high dynamic range imaging and 3D functions with depth up mode. Plants were imaged in their growth media, focusing on the cells at the center of the adaxial side of the cotyledon (fig. S1). The transient dehydration experiments were performed by imaging plants previously grown in 100% humidity in a dish with a lid open to the laboratory atmosphere and continuously illuminating with coaxial light. Rehydration was accomplished by natural plant response and adaptation.

Confocal Imaging and tissue expansion experiments

Samples were incubated in 550 mM sorbitol, 20 mM Tris, 0.5 mM CaCl₂, 150 mM NaCl, and imaged with a Zeiss LSM 710 laser scanning confocal microscope (Zeiss Oberkochen Germany). The cell wall was stained with 5 mM Calcofluor White (Sigma-Aldrich) for 5 minutes (1-3 razor cuts were performed to help staining and plasmolysis) and rinsed twice. The image was taken before the treatment followed by incubation at pH 7.5 with or without 0.1 μ L PME (Pectinesterase, from Orange Peel, Sigma P5400) or at pH 12 for 15 min or 2 h. The pH 12 buffer was the same as above, and the pH was adjusted to pH 12 with NaOH. The control experiments for pH 12 were performed in the same buffer, but at pH 7.5.

Immunohistochemistry

Immunohistochemistry was performed as described in (29). Fixation was performed using FAA buffer containing 50% ethanol, 10 % acetic acid, and 5 % paraformaldehyde followed by ethanol dehydration and incorporation into Paraplast (Sigma-Aldrich) with clearing by xylene. Tissue sections were performed using a microtome (Biotom Leica Wetzlar, 35578 Germany), and then sections were rehydrated. All of the steps were performed using a 2F4 specific buffer (20 mM Tris, 0.5 mM CaCl₂, 150 mM NaCl at pH 7.5). To label methylated pectins, we used the LM20 rat monoclonal antibody (PlantProbes Leeds UK, Cat. No. LM20). LM20 antibody requires methyl-esters for recognition of homogalacturonan and does not bind to un-esterified homogalacturonan (26). To label demethylated homogalacturonans, we used a 2F4 mouse monoclonal

antibody (PlantProbes Leeds UK, Cat. No. 2F4) recognizing the homogalacturonan domain that binds specifically to a dimeric association of pectic chains through calcium ions (27) with degrees of methyl-esterification up to 40 %. We have also used LM19 (PlantProbes Leeds UK, Cat. No. LM19) rat monoclonal antibody, that strongly binds to low-esterified homogalacturonans (26). We used the JIM7 (PlantProbes Leeds UK, Cat. No. JIM7) antibody to label partially methyl-esterified epitopes of the homogalacturonan (27). Secondary antibodies were an anti-rat or anti-mouse F(ab')₂ fragment tagged with Alexa Fluor 647 (which we abbreviate in the text as Alexa647) or CF568 dye. We used the following secondary antibodies: goat anti-mouse (Sigma Aldrich, SAB4600400) CF568 conjugated F(ab')₂ secondary antibody fragment; goat anti-rat (Sigma Aldrich, SAB4600086) with CF568 conjugated secondary antibody; goat anti-mouse (Strattech Scientific, 115-607-003-JIR) F(ab')₂ secondary antibody fragment conjugated to Alexa Fluor 647, and donkey F(ab')₂ anti-rat secondary antibody fragment conjugated to Alexa Fluor 647 (Abcam, ab150151).

Cryo-scanning electron microscopy (cryoSEM)

Sample preparation and image acquisition were performed as previously described in (43). High magnification imaging of cell walls was carried out on cotyledons that had undergone cycles of random cryo-fracture followed by screening for those rare fractures that occurred along walls of interest. Images were dependent on the fracture position, but only fractures occurring on the adaxial side and around the center of the cotyledons were analyzed (representative image of adaxial tissue sections are shown in fig. S2, A to C). CryoSEM data presented in Fig. 1, G and H and Fig. 3E were gathered from three independent experiments for WT and two for each PME13oe and PME5oe. For each independent experiment, we imaged two cotyledons for every condition, each one from a different seedling.

Cryo-scanning electron microscopy image analysis and filament width estimation

Linear regions of interest perpendicular to the observed filament long axes were drawn by hand in ImageJ. The data were then analyzed using Matlab (Mathworks, UK) custom-written script, which implements the findpeaks function. Due to the high background signal, the filament width was calculated as the full width at half prominence (see Matlab findpeaks documentation). Fibers with width below 10 nm were suppressed, which corresponds to the twice the average pixel size (the smallest structure observed has at least twice the sampling period, here the pixel size ~5 nm). We observed that the filaments with the width greater than 50 nm often represented fused multiple peaks, which were not correctly separated by the findpeaks function, and these were also suppressed, see fig. S6B. The Matlab scripts used in this section can be found here: DOI: 10.5281/zenodo.3581097. The updated version of this repository can be found here: <http://doi.org/10.5281/zenodo.3581097>.

Direct Stochastic Optical Reconstruction Microscopy (dSTORM)

dSTORM was performed with a buffer containing 100 mM MEA-HCL (Sigma, M6500), 10 % glucose (Sigma), 0.5 mg/ml glucose oxidase (Sigma, G2133) and 40 µg/ml catalase

(Sigma, C100) in 2F4 buffer at pH 7.5. Samples were imaged at room temperature in sealed 8-well ibidi μ -Slides (Ibidi, 80821) by direct STORM on an inverted N-STORM microscope (Nikon Ti, Japan) with an Apochromat 100x/1.49 NA oil immersion objective. Images were acquired in highly inclined illumination mode, and focal drift was prevented with hardware autofocus (Nikon Perfect Focus System). CF568 and Alexa647 were first pumped in their dark state using the 640 nm (~150 mW) and 561 nm (~90 mW) laser lines at maximum laser intensity and then continuously acquired. Three dimensional (3D) dSTORM was achieved using an astigmatic lens placed in front of the camera. Z-calibration and warp calibration were performed using 100 nm multicolor fluorescent microbeads (Tetraspeck, Invitrogen). Data were acquired with a field-of-view (FOV) 256x256 pixels (160 nm pixel size), at 65 frames per second typically for 25,000 frames with cooled (-70 °C) EMCCD camera (iXon Ultra DU897, Andor). CF568 was always acquired sequentially to Alexa Fluor 647, utilizing a Quad-Band Set for TIRF applications (Chroma, TRF89901, ET – 405/488/561/640 nm) and the ET600/50 nm and ET645/75 m for 647 emission filters (Chroma) to reduce cross-talk between the detection of the two fluorophores. Experiments were performed on plants 3 days post-germination. The cuts were selected to contain adaxial epidermal cells with external periclinal cell wall to middle epidermal layer section cuts, from the center part of the cotyledons, as shown in a representative cut, fig. S2, A to C (the full cut could only be observed using confocal imaging). The deeper cuts were not used, fig. S2, D to F. The curvature of the cotyledon facilitates the distinction of the adaxial and abaxial cells, compare fig. S2, A to C, and fig. S2, J to L, as well as the deeper cotyledon layers, fig. S2, G to I. Only cuts presented in fig. S2, A to C were imaged using dSTORM. The data presented in Figs. 1 and 2 represent 12 independent experiments (biological replicates defined as different plants, tissue preparation, immunolabeling) with at least one cotyledon prepared for each condition.

dSTORM data analysis

Single-molecule localization analysis was performed with the Nikon N-STORM software setting the maximum possible width of a spot to 700 nm and the maximum axial ratio (ratio of elongation in X- and Y- directions) to 2.5. The 100 nm multicolour fluorescent microbeads were used as fiducial markers to register the two channels, as well as for Z-position calibration and chromatic aberration corrections. Lateral drift was automatically corrected using a correlation algorithm on molecular locations between successive frames. The remainder of the data analyses were performed by a custom Matlab-based Grafeo program (<http://doi.org/10.5281/zenodo.3663608>) or at <https://github.com/inatamara/Grafeo-dSTORM-analysis> to get the latest version. Plant tissue has strong autofluorescence, which contributes to elevated background detection. However, dSTORM buffer is optimized for the specific dyes; hence, background fluorescence is typically weaker than the signal. Therefore, the single-molecule localization data was first filtered based on the number of photons emitted by a molecule and the localization precision. Background detection is often less organized and can be further filtered based on 3D Voronoi diagrams, as described previously (44).

HG nanofilament width estimation from 3D-dSTORM data

The data analyses were performed with a custom Matlab-based Grafeo program. Point clouds, the coordinates of localized emitters, were segmented using 3D Voronoi diagrams (VD) and two-dimensional Delaunay triangulation (DT) thresholding (39). DT was represented as bidirectional graphs containing points connected with edges. The points were assigned to discrete clusters (filaments), connected components, by removing all DT edges larger than typically 50 nm and also by removing graph nodes (points) with a degree (number of connections) typically smaller than 5. These values varied slightly depending on the noise level. DT edge thresholding permitted to disconnect closely spaced structures that are connected by longer edges than intracluster edges. The width of a filament was calculated as the median of all two dimensional (i.e., in lateral dimensions, X and Y) pairwise distances between filament radial centroid and all the localization belonging to the same graph.

HG methylation asymmetry analysis

The HG methylation asymmetry in the anticlinal walls; first, straight and lobed regions were annotated manually in the Grafeo program. The linear or curved line segments were drawn manually between two cell walls, and the program drew automatically two regions of interest on each site enclosing two adjacent cell walls (see Line segment ROI and related functions in Grafeo v.2 manual). HG methylation asymmetry was then calculated as the ratio of the number of detected LM20 or 2F4 epitopes in the convex and concave part of a cell wall for a lobed wall segment or the two sides of a wall in case of a linear wall segment. The HG methylation asymmetry in the periclinal walls; first, two closed, polygonal regions of interest were drawn in the convex and concave region in the lobed region of the cell. As the topography of a periclinal wall at the junction with the anticlinal wall is different on each side, and 3D-dSTORM Z detection range is ~750 nm, it is not always possible to detect signal in the concave and convex regions of periclinal walls for the same lobe, as it is for the anticlinal walls. Therefore, the HG methylation asymmetry for periclinal walls was obtained as the ratio of the number of detected 2F4 to LM20 epitopes for each of the two regions of interest (convex and concave) separately.

Statistical analysis

Statistical test of significance was performed in Matlab using multiple group comparison method (see Matlab multcompare function documentation) with the Kruskal-Wallis test. This non-parametric test was used since compared data didn't meet the normality assumption. P-values were adjusted using Bonferroni correction.

Digital time-lapse image analysis

Image analysis and segmentation were performed in Matlab using custom-written scripts. First, the coherence filter (available at Matlab exchange website) was applied to enhance curvilinear edges, followed by adaptive thresholding and extraction of the brightest contour pixels. Images acquired in the consecutive days were rescaled, translated, and rotated before tracking. Then individual cells were followed based on the nearest neighbor distance between centroids of the cells in the consecutive images. Next, cellular

contours were extracted and transformed from Cartesian to polar coordinates using the centroid to periphery distance, which we call radius. The cellular shape spectra were obtained by the spatial Fourier transform of the radius. The primary and secondary undulations were identified based on the frequency composition of the shape spectra. As the cell grows, the absolute value of the spatial frequency corresponding to the same lobe/oscillation number is increasing. Therefore, to facilitate the tracking of the same undulations between consecutive days and identification of new frequencies, we calculated frequency normalized to the fundamental frequency, i.e., corresponding to the shortest spatial oscillation along the cellular contour. In this picture, the spatial frequency of 1 (the fundamental v_0 divided by itself) corresponds to an oval-shaped or elongated cell, whereas a circular cell has a spatial frequency equal to zero. The number of undulations is equal to twice the normalized frequency $v_n = 2*v/v_0$. The presence of given normalized frequency v_n in shape spectra highlights the undulation with a frequency $v = v_n*v_0/2$. The integrated energy of the peak in the Fourier spectra was calculated as the Power Spectral Density (PSD) so that Parseval's identity is fulfilled. It was obtained with following formula $\sum \mathbf{FT}^2 \cdot d\mathbf{f}/2$, where \mathbf{FT} is a Fourier Transform of the radius (shape spectra), $d\mathbf{f} = \mathbf{F}_s/\mathbf{N}$, \mathbf{F}_s is a sampling frequency (inverse of image pixel size), \mathbf{N} is a number of points in the contour. For each peak, the sum operator (\sum) runs over $\mathbf{P}_{\max} \pm w$, \mathbf{P}_{\max} is a frequency at peak maximum, and w is a peak width. The Matlab scripts for cell tracking and shape analysis can be found here: <http://doi.org/10.5281/zenodo.3665413>. The latest version of this repository can be also followed here: <https://zenodo.org/badge/latestdoi/197577846>, or here: <https://github.com/inatamara/ShapeSpectraAnalysis>.

Tissue expansion analysis

The tissue expansion measurements were performed using ImageJ (ImageJ 1.5s), using two different methods: by measuring the change in the distance between 10 independent pairs of reference points visible on the same Z section before and after treatment; and also as the change in the cell area before and after treatment, fig. S10B.

Finite Element Method Modelling

Finite method element modeling was performed with custom-written Matlab scripts. We implemented a 3D nonlinear elastic finite element model (FEM) using an 8-node brick element with 24 degrees of freedom with full integration. The continuous mechanics problem was solved using a total Lagrangian approach (31). The isotropic hyperelastic material model was implemented, where the strain energy density function was given by a three-parameter compressible Mooney-Rivlin material as described in (31):

$$W(J_1, J_2, J_3) = A_{10} \cdot (J_1 - 3) + A_{01} \cdot (J_2 - 3) + A_{11} \cdot (J_3 - 3)^2 \quad (1)$$

Where the J_1, J_2, J_3 are reduced invariants of right Cauchy-Green tensor $\mathbf{C} = \mathbf{FF}^T$ and \mathbf{F} is a deformation gradient. The idealized two cell junction was modeled with two periclinal walls connected with the single anticlinal wall, fig. S7A. To account for the growth, the total deformation gradient was multiplicatively decomposed into a growth deformation

tensor, \mathbf{F}_g , and an accommodating elastic deformation tensor \mathbf{F}_e : $\mathbf{F} = \mathbf{F}_g \mathbf{F}_e$ (fig. S7), (32). At every growth iteration, each solid brick element in the body is grown independently according to the law described in the section below. Such incompatible growth, \mathbf{B}_{t1} , may lead to discontinuities and overlaps between the parts of a body (fig. S7B). The elastic deformation assembles all the elements into the compatible grown body \mathbf{B}_t . It is assumed that the accommodating elastic deformation is instantaneous to growth deformation so that the later can be considered a virtual state. Furthermore, the growth process occurs at a much slower time-scale compared to elastic equilibrium; hence, it can be assumed that at each growth step, the body is in equilibrium. The incompatible growth state is, by definition, stress-free so that all the stresses arise due to accommodating elastic deformation and external forces. We assume that stresses due to accommodating elastic deformation are relaxed between successive growth step, by the processed of a cell wall remodeling, which is not explicitly modeled. This allows for the assumption that at the start of each growth iteration, the stresses due to internal body forces are negligible so that an evolving initial grown state is a compatible growth state without external loads applied. Given the growth deformation gradient, the unknown at each iteration is the nodal displacement vector \mathbf{u} due to total elastic deformation. The solution of nonlinear problem consists of solving a variational equation for unknown nodal displacements \mathbf{u} , derived from equating virtual work performed by internal body forces and a virtual work performed by external loads.

The growth laws for the anticlinal wall. At each growth iteration, the nodal displacements due to local growth of an anticlinal wall element are given by:

$$g_{Ax}(x,y) = D_{exo} (W_p + D_{dmet}^{L,R}(x,y) P_{XY})/2 \quad (2)$$

$$g_{Ay}(x,y) = D_{exo} D_{dmet}^{L,R}(x,y) P_{XY} L_{ij}/2 \quad (3)$$

$$g_{Az}(x,y) = D_{exo} D_{dmet}^{L,R}(x,y) P_z L_{ij}/2 \quad (4)$$

Where $g_{Ax}(x,y)$, $g_{Ay}(x,y)$ and $g_{Az}(x,y)$ are the local nodal displacements in X, Y and Z direction, respectively, D_{exo} is the exocytosis rate, and $D_{dmet}^{L,R}(x,y)$ is a local demethylation rate (x,y, corresponds to the position along and across anticlinal wall), respectively for left (L) or right (R) element (fig. S7). $P_{XY} = W_p(1.42 - 1) = 0.35$ nm is a demethylation-induced pectin polymer lateral expansion, where $W_p = 0.837$ nm is the width of a single pectin polymer, and $P_z = 1.327 - 1.34 = -0.013$ nm is a contraction along axial dimension. The L_{ij} is a relaxed edge length connecting node of interest with its neighbor, e.g., for the displacement of nodes 1 or 2 (fig. S7) in the X-direction, it is the edge L_{12} . For the middle (M) anticlinal wall nodes 2, 3, 6, 7, follow the equations for the right (R) anticlinal wall, and the nodes 1, 4, 5, 8 the equations for the left (L) anticlinal wall (fig. S7A).

The growth laws for the periclinal wall. At each growth iteration, the nodal displacements due to growth of a periclinal wall element are given by:

$$u_{Px,y} = D_{exo} D_{dmet}^P P_{XYZ} L_{ij}/2 \quad (5)$$

$$u_{Pz} = D_{exo} (W_p + D_{dmet}^P P_{XYZ})/2 \quad (6)$$

Where D_{dmet}^P is the demethylation rate for the periclinal wall and $P_{XYZ} = (2P_{XY} + P_Z)/3 = 0.22$ nm is an average pectin expansion in three dimensions. For periclinal walls, P_{XYZ} is used, since HG polymers are oriented randomly and do not form nanofilaments. HG expansion rates due to demethylation were calculated using the parameters from (20) and were obtained as follows. Methylated HG forms a hexagonal lattice with a unit cell side length $a = 0.837$ nm in the X and Y plane and a helical repeating unit of 1.34 nm in the Z-direction. Upon demethylation, HG forms a rectangular lattice with unit cell dimensions $b = 0.99$ nm and $c = 1.23$ nm and a helical repeating unit of 1.327 nm in the Z direction. Then the average HG expansion in lateral dimensions E_{XY} was obtained as $\sqrt{A_r/A_h} = 1.42$, where $A_r = bc$, is an area of the rectangular unit cell, and $A_h = a^2 \sqrt{3}/2$ is an area of the unit cell of a hexagonal lattice. We tested different coarseness of a mesh with a variable number of elements and used the minimal number of elements that would assure a stable solution. The 3D elements are computationally expensive; hence, we chose the smallest number of elements across the walls: three for the anticlinal wall and two and one for the top and bottom periclinal wall, respectively. This corresponds well to reality since, in pavement cells, the periclinal walls are thinner than anticlinal walls by roughly 30 %. For simplicity and without losing generality, the bottom periclinal wall had only 16 degrees of freedom, and the nodal displacements in the Z-direction were restricted. The HG demethylation rates, $D_{dmet}^{L,R}(x,y)$ and D_{dmet}^P , were derived from dSTORM data, Fig. 2, B and C, and fig. S8 and S9. For the periclinal walls, D_{dmet}^P was 0.6, 0.9, 0.05 for WT, pectin methyltransferase overexpressor (PME5oe), and pectin methyltransferase inhibitor overexpressor (PMEI3oe) cotyledons respectively. The anticlinal walls in the WT cotyledons had 0.61, 0.57, and 0.41 for straight walls (two sides), convex and concave side of the wall respectively; 0.9 and 0.05 in PMEI3oe and PME5oe cotyledons. The local demethylation rates, $D_{dmet}^{L,R}(x,y)$, along R and L anticlinal walls, were interpolated as one-period sinusoids with 0.61 at the extremities, and 0.57, and 0.41 at the maximum and minimum, respectively. The exocytosis rate was set to 0.05 unless stated otherwise. The following Mooney-Rivlin parameters were used: $A_{10} = 10$ pN/nm², $A_{01} = 1$ pN/nm² for both anticlinal and periclinal walls. The third parameter, A_{11} , controlling the compressibility, was set to 100 pN/nm² and 1 pN/nm² for anticlinal and periclinal wall, respectively. The model refers to aligned HG nanofilaments present only in the anticlinal walls. Therefore the compressibility of periclinal walls was lower compared to the anticlinal walls. However, for simplicity, we kept to an otherwise spatially isotropic material model. The turgor pressure was applied normal to the surface of the element face directly facing the cytoplasm and was set to 0.25 MPa. The Matlab implementation of the model can be found here: <http://doi.org/10.5281/zenodo.3664101>. The latest version of this repository can be also followed here: <https://zenodo.org/badge/latestdoi/197578315>, or here: <https://github.com/inatamara/FEMmodelPavementCells>.

Supplementary figures

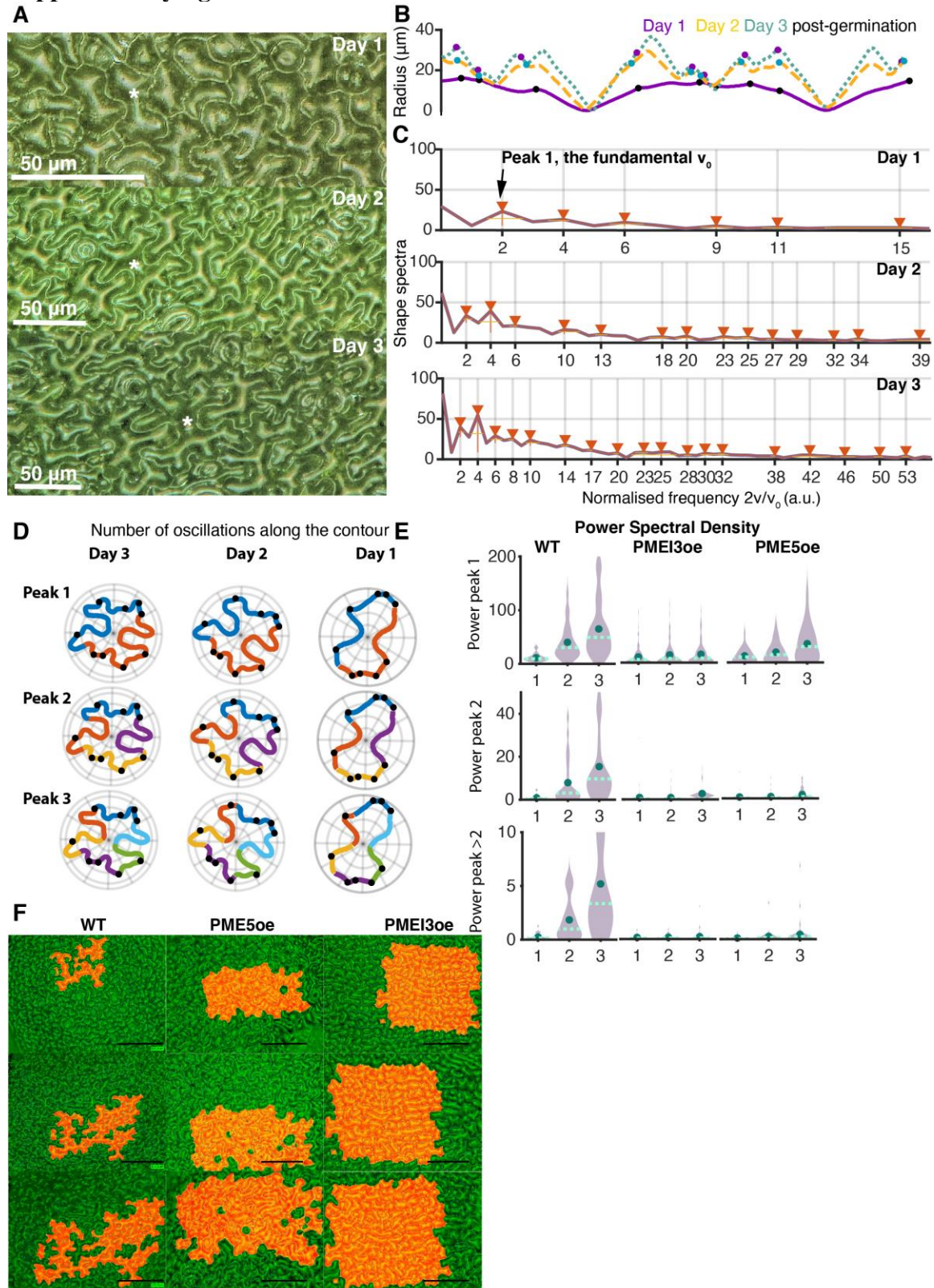


Figure S1: shape spectrum analysis of growing pavement cells.

(A) Digital time-course imaging of *Arabidopsis thaliana* (ecotype WS) cotyledons. Day 1, 2, and 3 mark days after germination. The white star highlights the same cell in the consecutive images. (B) Polar coordinate representation of cell (the same as in A) contours; the radius is the distance from center-of-area to point on the contour. Solid violet, dashed orange and dotted green curves represent day 1, 2, and 3 after germination, respectively. The colored dots on the curves mark the location of tri-cellular junctions. (C) The shape spectra, Fourier transforms of radii from B. The shortest oscillation (the highest frequency) represented on the three graphs is $\sim 6 \mu\text{m}$ (see also supplementary Audio file 1). (D) Representation of the shape spectra as the number of oscillations along the cell contour. Color-coded segments aide visualization, and black dots mark the location of tri-cellular junctions. The peaks 1, 2 and 3 correspond to the peaks at the normalized frequencies (number of oscillations) 2, 4, 6 in C. (E) The integrated energy (Power Spectral Density, PSD, see Material and Methods) under the first, second and all remaining peaks summed together in wild type (WT), PME5oe and PMEI3oe. (F) Digital microscope time-course imaging of WT, PME5oe, and PMEI3oe cotyledons; day 1, 2, and 3 mark days after germination. Cells, which were followed over three days, are highlighted in red. The division of mature, differentiated pavement cells was not observed in any condition. We did observe the successive asymmetrical division of the small meristemoid cells and their differentiation into guard cells. Over the course of experiments (three days), we estimated 44 % of the small meristemoid cells in the WT plants divided, ~ 20 % in PME5oe, and ~ 4 % in PMEI3oe.

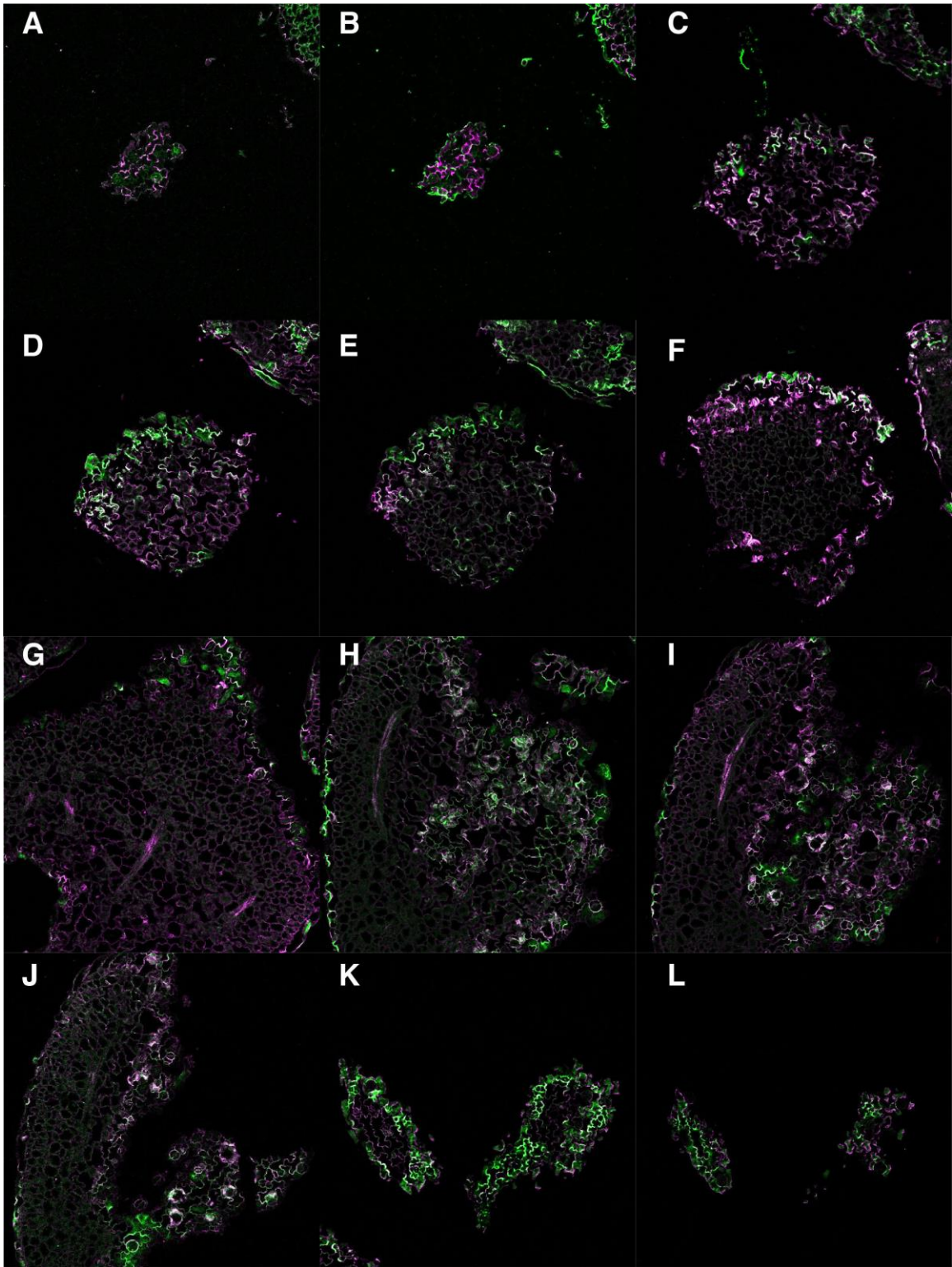


Figure S2: Overview fluorescence images showing how cotyledon tissue sections were selected.

Homogalacturonans were labelled with the following antibodies: LM20 antibody against methyl-esterified homogalacturonan (magenta) and 2F4 antibody against demethylated homogalacturonan (green).

In this study, we looked only at the adaxial and not abaxial epidermal pavement cells. The adaxial and abaxial epidermal tissue cuts can be differentiated based on the shape of tissue sections, as described below. (A-C) Consecutive epidermal tissue cuts with adaxial cells, including external periclinal cell wall to middle epidermal layer sections. As the adaxial surface is curved, the central part of the cotyledons is present as a tissue section smaller than the entire organ. These adaxial sections represent the region of the cotyledon that were utilized for dSTORM analysis. (D-F) Consecutive epidermal cuts from the middle section to the bottom (abaxial) periclinal wall. In (F), the deeper tissue layers are visible in the center of the cut. (G-I) Central sections of the cotyledon, including only deeper cellular layers and no epidermis. (J-L) Abaxial epidermal sections present different curvature from the adaxial part resulting in noncontiguous pieces of the tissue in individual sections. All the tissue sections are ~4 μm thick.

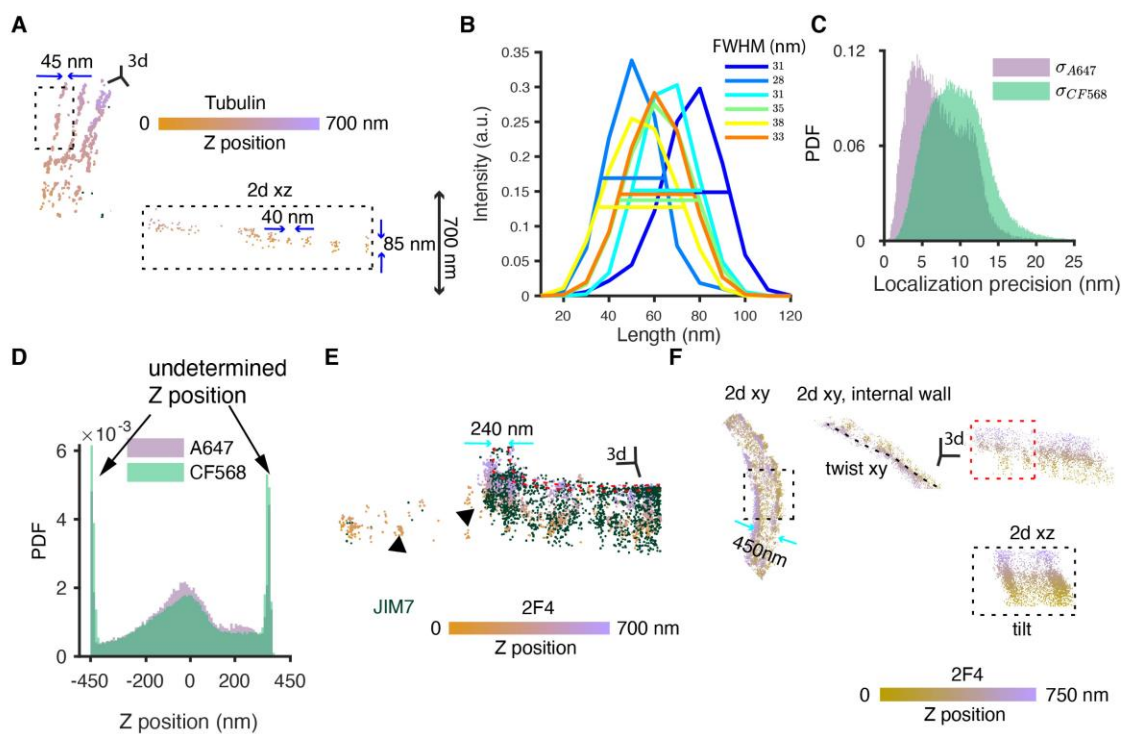


Figure S3: The 3D-dSTORM resolution evaluation.

(A) The 3D-dSTORM image of microtubules used to assess the resolution limit. (B) Cross-sectional Full Width at Half Maximum (FWHM) of the microtubules used to estimate the 3D-dSTORM lateral resolution, where color-code represents selected representative microtubules. Cross-sections of selected microtubules are shown with FWHM highlighted as a horizontal line and a number indicating FWHM in nanometers. (C) Probability density function (PDF) distributions of the lateral localization precision of the two fluorophores used in this study Alexa647 and CF568. Lateral localization precision for x and y dimensions and combined ($\sigma = \sqrt{\sigma_x^2 + \sigma_y^2}$) lateral localization precision were computed as previously described in (38). (D) Example distribution of the Z-position of the epitopes tagged with Alexa647 and CF568 fluorophores. The two sharp peaks at the two extremities of the plot correspond to localizations with an undetermined Z-position, which are typically too dim to be properly localized, or their position lies outside of the range (~400 nm at each side of a focal plane). The broad peak in the middle indicates that due to variable signal-to-noise ratio at different Z-positions, the highest number of points is detected when the molecule is located around the focal plane, and the efficiency of detection drops down for the epitopes away from the focal plane. For this reason, the density of points in the 3D STORM data plot is the highest at the center of the detection range. (E) The 3D-dSTORM image showing the demethylated HG revealed with 2F4 antibody (orange-violet encoding for Z-position) and partially methylated HG revealed with JIM7 antibody (green). Black arrowheads mark small clusters at the lowest Z-position corresponding to isolated secondary antibodies on the glass. The extension in the axial dimension (Z) of such clusters is much smaller than HG nanofilaments, showing that the latter are not an artifact of 3D-dSTORM imaging. (F) The 3D-dSTORM image showing the demethylated HG 2F4 epitope (orange-violet encoding for Z-position). The presented wall segment is slightly tilted away from the Z-axis showing inclined HG nanofilaments. Part of the wall is also twisted in the XY plane, and the HG nanofilaments follow the twist. These observations also indicate that the HG nanofilaments are not an artifact of 3D-dSTORM.

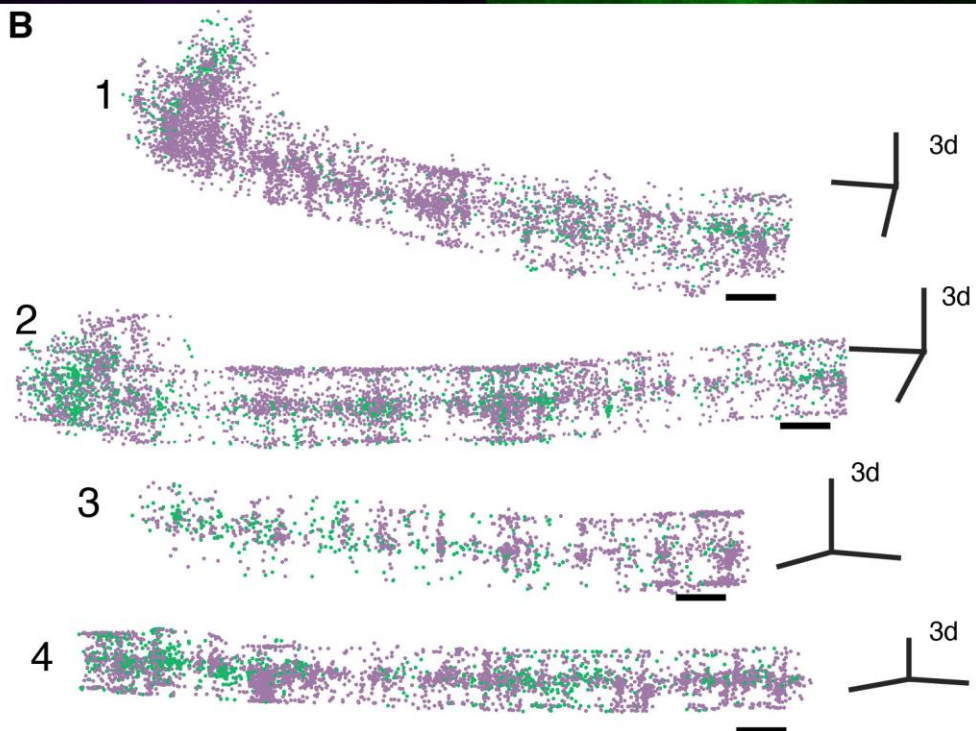
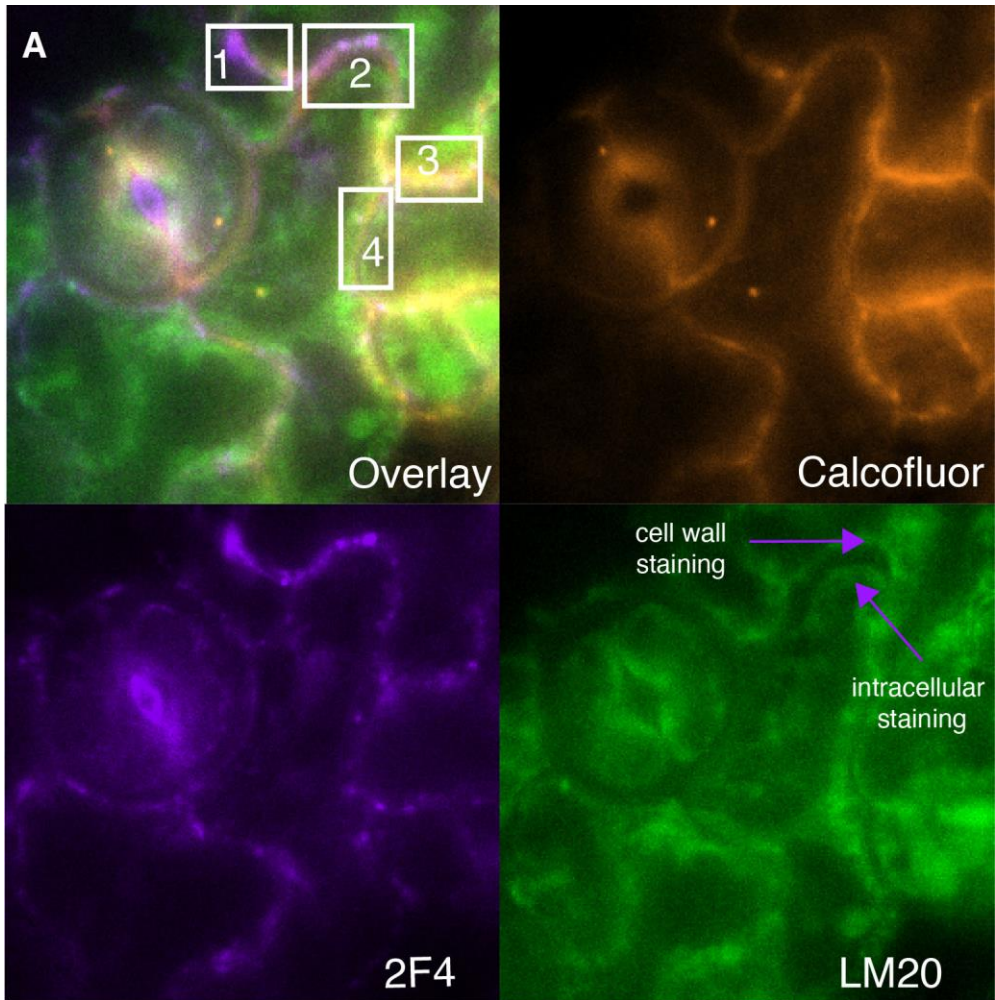


Figure S4: The 3D-dSTORM imaging of young WT cotyledons (1-day post-germination).

(A) Low-resolution image of WT cotyledon epidermal tissue section acquired 1-day post-germination labelled with LM20 and 2F4 antibodies against methylated and demethylated HG, respectively, and Calcofluor White dye for the general cell wall staining. At 1-day post-germination LM20 presents a high level of intracellular staining, pronounced in the vicinity of the cell wall. Part of the signal may be generated by nonspecific autofluorescence. (B) The 3D-dSTORM images of the wall segments highlighted with white boxes in (A) showing the fibrous pattern in the anticlinal walls. Scale bar, 1 μm .

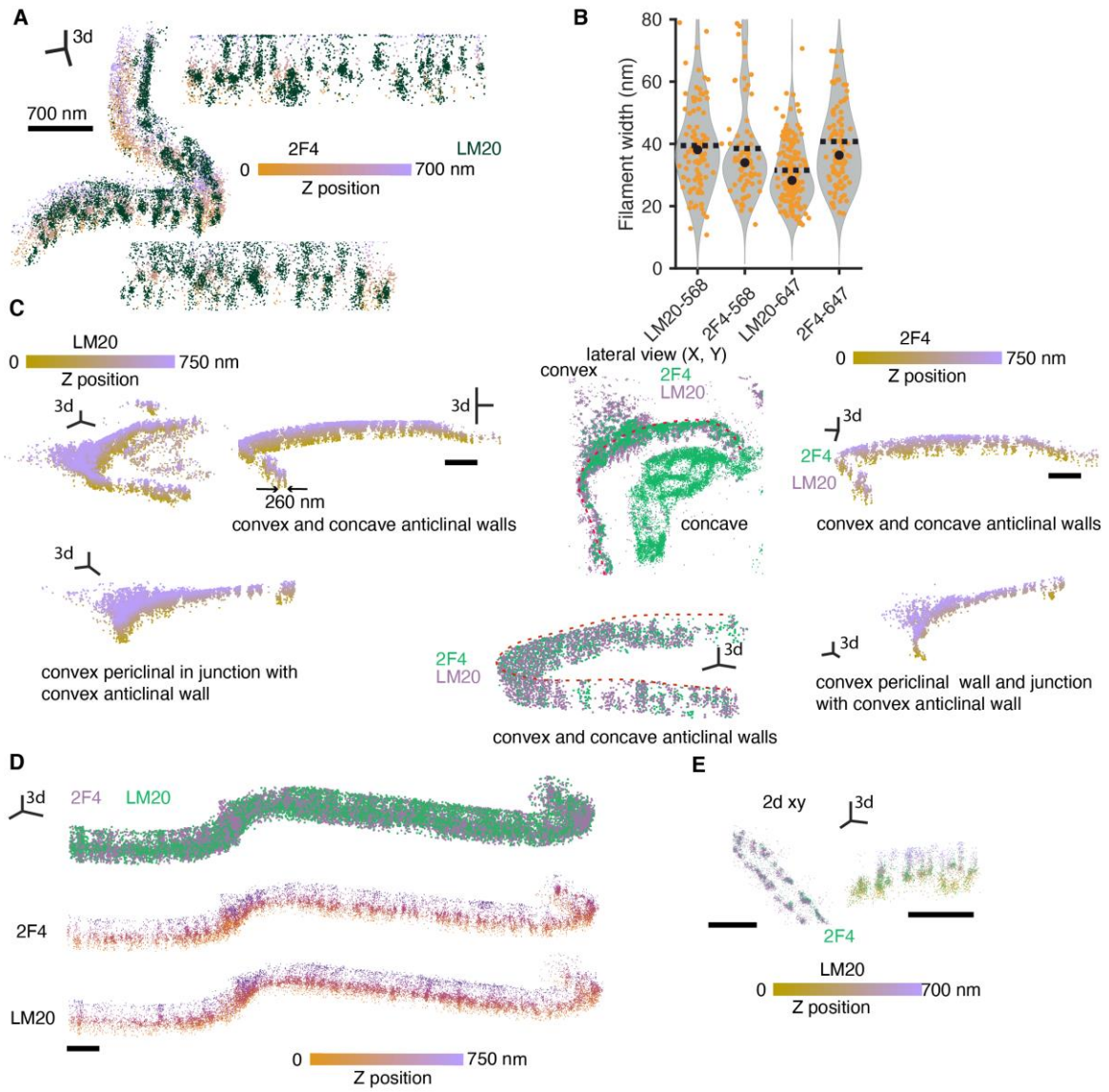


Figure S5: dSTORM imaging of the WT Arabidopsis cotyledon pavement cells.

(A) The same wall segment as in Fig. 1C, but here 2F4 antibody is represented using a colormap to encode the Z-position; LM20 shown in dark green. (B) The same data as shown in Fig. 1D, but represented for each secondary antibody fluorescence tag (Alexa647 and CF568) separately. (C) Color-coded Z-position of methylated HG epitope LM20 (left), demethylated HG epitope 2F4 (right) and overlay of LM20 (violet) and 2F4 (green) epitopes (middle) in the lobed region of pavement cells showing the staining in the anticlinal walls and the anticlinal walls in junction with a periclinal wall. At the junction of the anticlinal and periclinal walls, the filamentous organization of HG gradually disappears. (D) Swapped secondary antibody tagging LM20 (CF568) and 2F4 (Alexa647) as compared to the data presented in Fig. 2, B and C, showing that both LM20- or 2F4-labelled filaments are usually better resolved when the Alexa647 probe is used. (E) The 3D-dSTORM image showing the methylated HG LM20 epitope (orange-violet encoding for z-position) and demethylated HG 2F4 epitope (green) of straight cell wall segment in the pavement cells with visible HG nanofilaments.

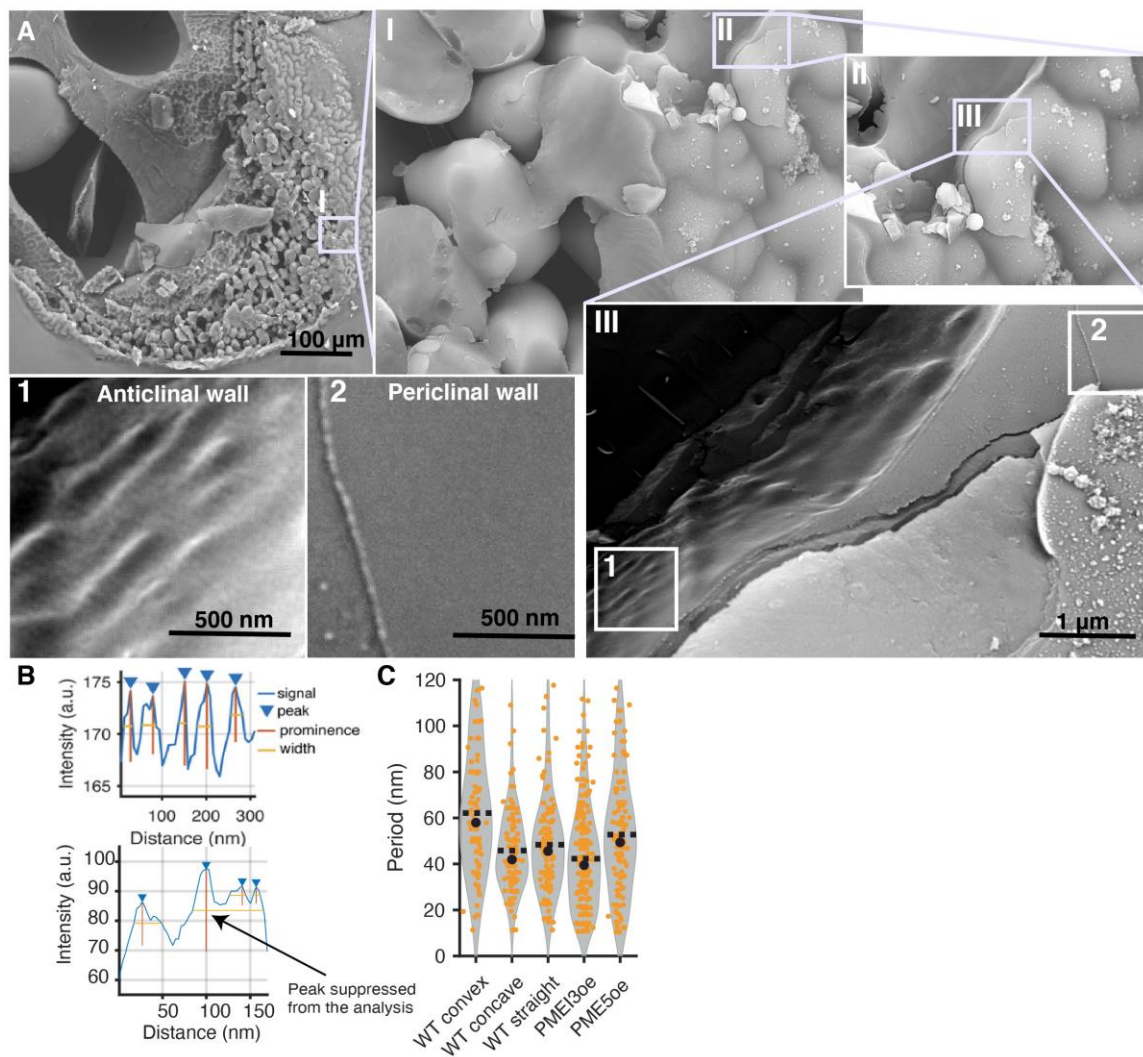


Figure S6: Successive zooming steps of the walls of interest imaged with cryo-fracture SEM.

(A) Cryo-fracture SEM images showing successive steps of enlargement of the pavement cells to explain how cell wall regions of interest were identified as the periclinal wall, anticlinal convex, anticlinal concave or straight wall. The regions labeled one and two show anticlinal and periclinal walls, respectively. Filamentous features can be distinguished in the anticlinal wall but not in the periclinal wall. (B) The representation of the analysis of the filament width in the cryo-fracture SEM images (top). First, a linear region of interest perpendicular to the axis of the filament was drawn using Image J. Then Matlab findpeaks function was used to detect peaks, estimate their features like width and location. Here we report filament width as the width at the half prominence (see Matlab documentation of findpeaks function and SEMfilaments Matlab scripts associated with this publication). The bottom graph shows an example of a broad, composed peak, which was suppressed from the final analysis. (C) The distribution of the filament interspacing in the cryo-fracture SEM images.

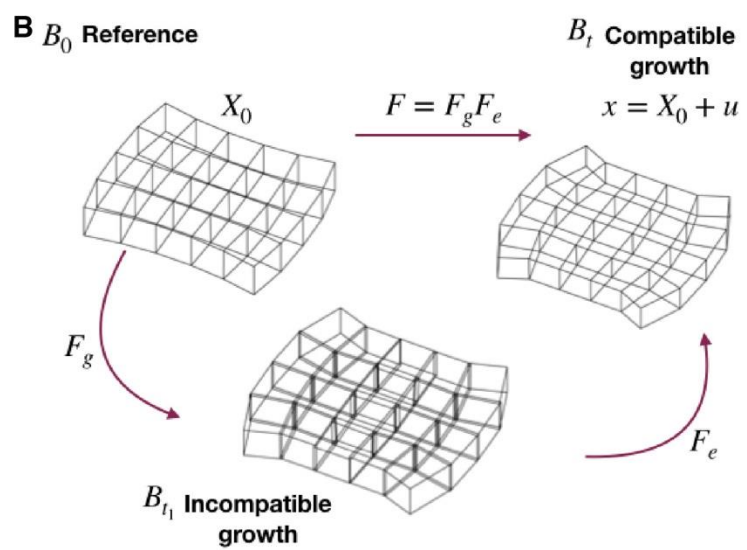
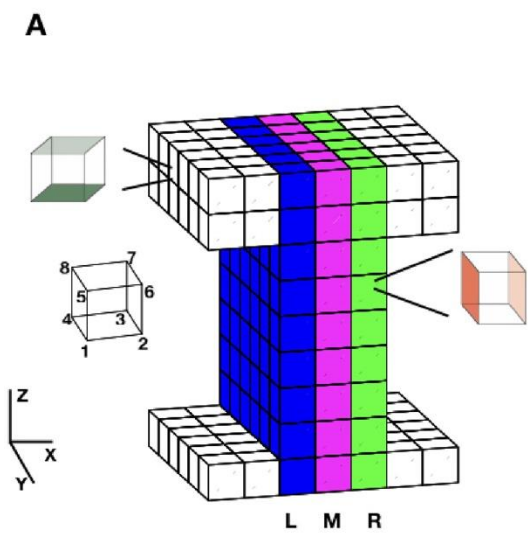
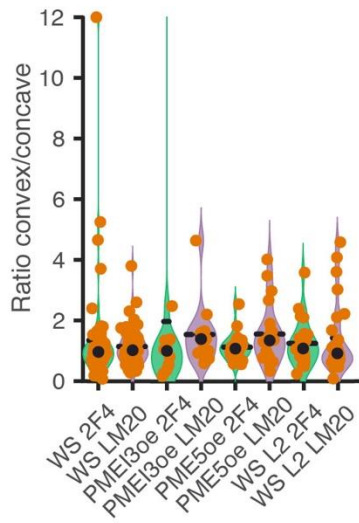


Figure S7: Finite Element Method model for the lobe formation.

(A) Miniaturized mesh used for the FE model. The anticlinal wall has a three-element thickness: left (L), right (R), and middle (M). The bottom and top periclinal walls have a thickness of one and two elements, respectively. (B) Schematic representation of an FE model of growth. At each growth iteration, total deformation gradient \mathbf{F} transforms the initial body \mathbf{B}_0 with the nodal position vector \mathbf{X}_0 into \mathbf{B}_t state with the nodal position vector \mathbf{x} , where \mathbf{u} is a nodal displacement vector. The vector \mathbf{u} includes nodal displacement due to a known growth deformation gradient \mathbf{F}_g and the unknown accommodating elastic deformation gradient \mathbf{F}_e for which optimization problem is solved. The \mathbf{B}_{t1} state corresponds to incompatible growth, or relaxed state (Fig. 3D), before application of the accommodating elastic transformation \mathbf{F}_e , which connects all the elements back together. The \mathbf{B}_{t1} state can be used to estimate the width of the cell wall in the absence of the tissue stress, for instance, after the tissue pre-treatment and preparation for TEM or dSTORM imaging leading to (at least partial) stress relaxation.

A

Straight walls

**B**

Buckled walls

Straight walls

secondary antibody swap

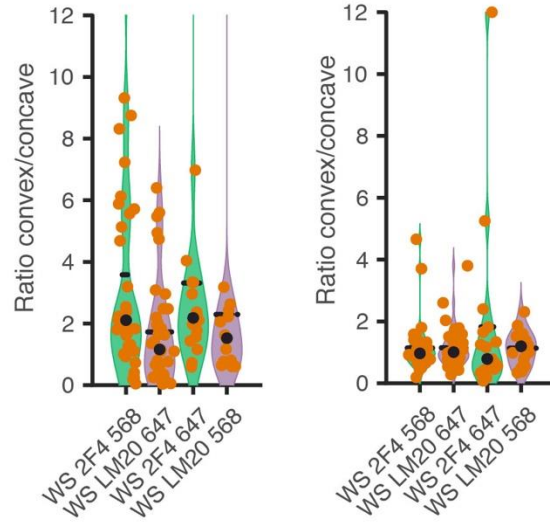


Figure S8: The quantification of HG methylation asymmetry.

(A) The HG asymmetry in the straight anticlinal walls of pavement cells in WT, PME5oe, and PMEI3oe cotyledons. (B) Comparison of the HG asymmetry for swapped secondary antibodies Alexa647 and CF568 either LM20 or 2F4 epitopes in the lobed and straight anticlinal walls, respectively.

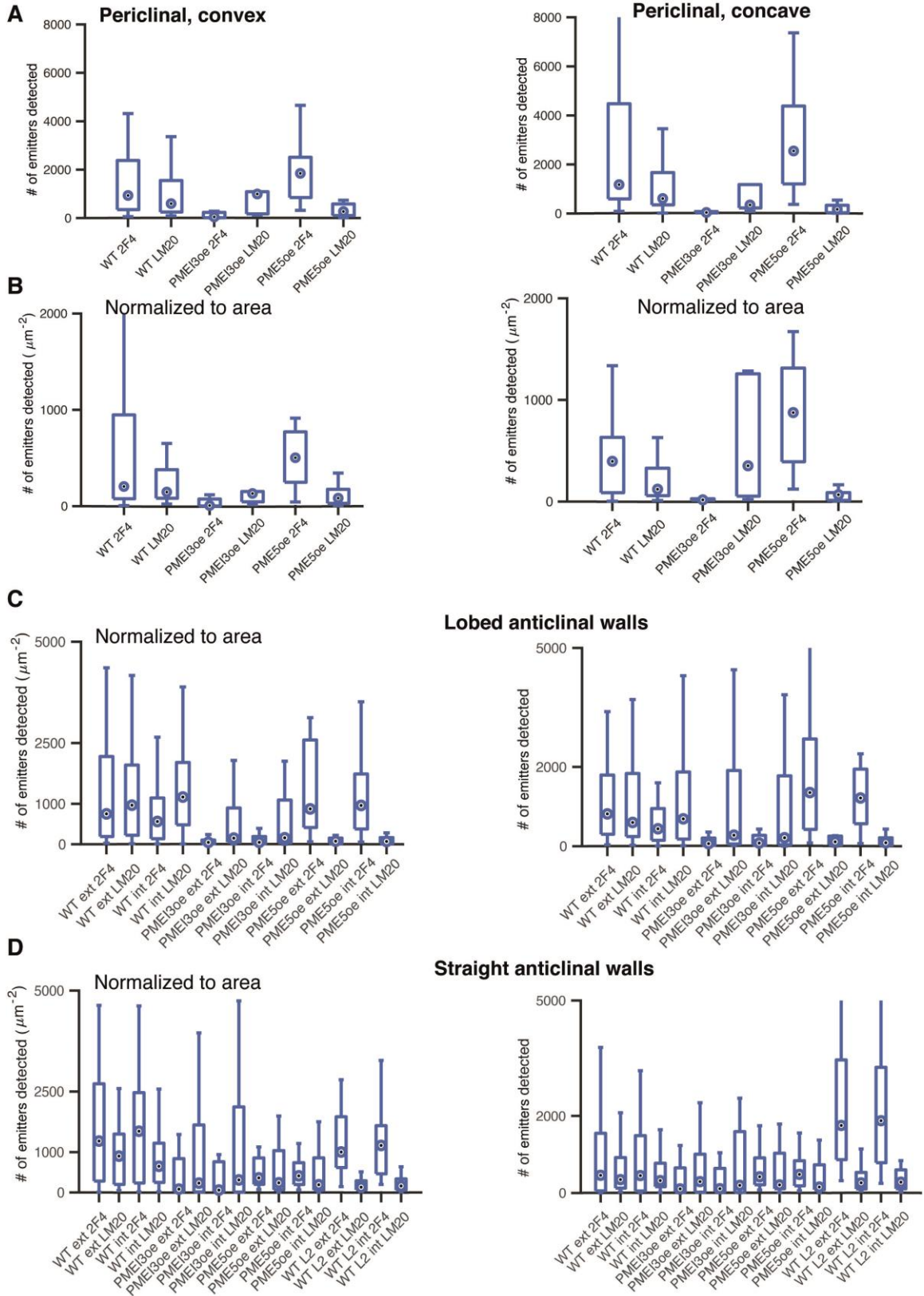


Figure S9: Raw data for the quantification of HG methylation asymmetry shown in Fig. 2, B and C, and Fig. S8.

(A) The number of detected emitters (fluorophores tagging LM20 or 2F4 antibodies) in the region of interest (ROI, see Material and Methods for details), in the convex (left) and concave (right) part of a lobe in the periclinal wall. (B) The same as in A, but normalized to the area of the ROI. (C) And (D) The number of detected emitters on the two sides of the anticlinal wall normalized (left) or not (right) to the area of the ROI in lobed and straight walls, respectively. The data presented here are raw data (the counts), as compared to ratios shown in Fig. 2, B and C presenting methylation asymmetry calculated as described in the Materials and Methods.

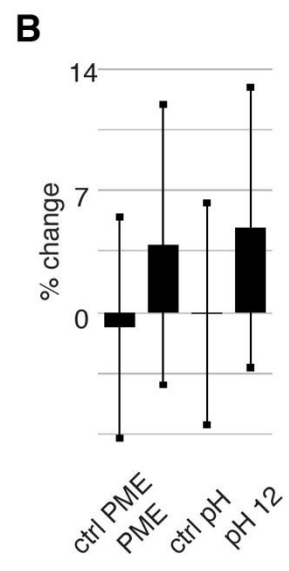
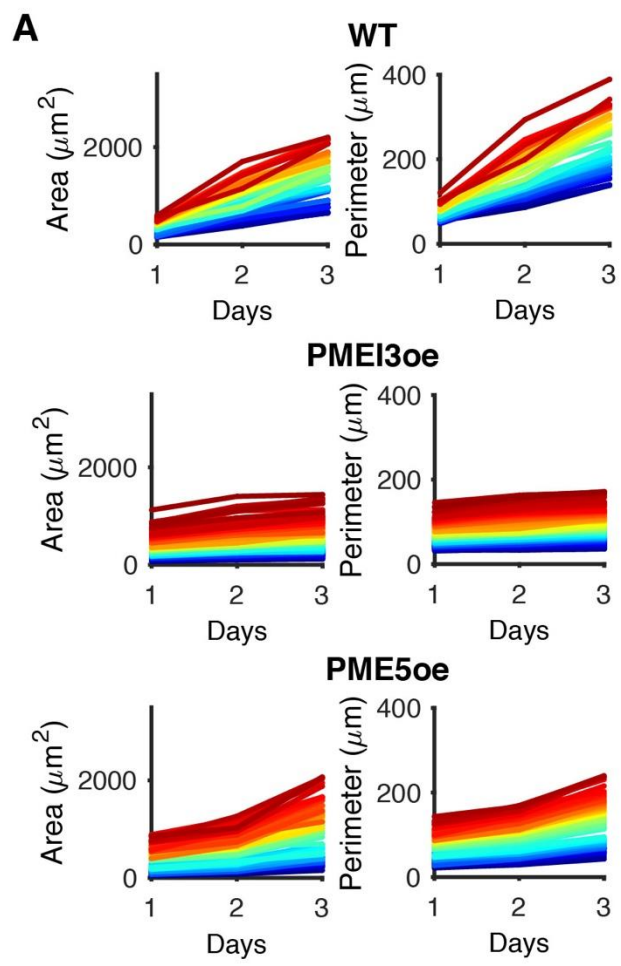


Figure S10: Evaluation of PME5oe and PME13oe impact on lobe formation.

(A) Progression of the area and the perimeter of pavement cells across three days of time-lapse experiments acquired with a Keyence VHX-5000 digital microscope in WT, PME13oe, and PME5oe cotyledons. For display purposes, cells were sorted according to their area and color-coded from the smallest (blue) to the largest (brown-red). (B) The quantification of tissue expansion upon HG demethylation with PME enzyme or with a pH 12 buffer measured as the percentage (%) change in the average cell area in all repeats after the treatment. Y-axis is % change in measured size before and after given treatment, and graphs represent mean \pm STD (standard deviation).

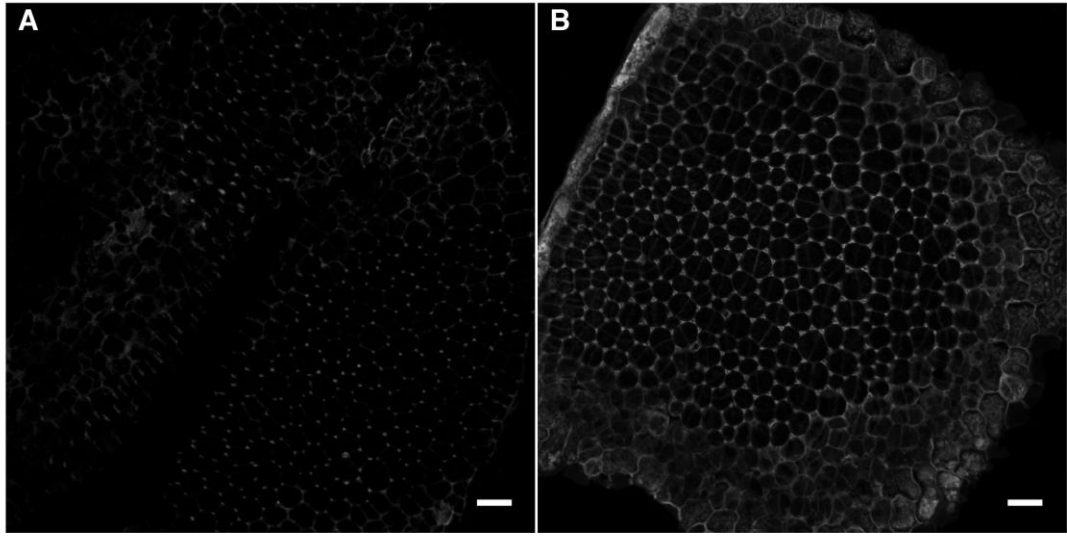


Figure S11: The pH 12 buffer leads to demethylation of homogalacturonan.

(A) Immunolabelling of low-methylesterified HG after 15 min treatment with the buffer at pH 7.5 or (B) at pH 12. After 15 min incubation at pH 12, the staining against demethylesterified HG is higher than in control experiments and is localized to the cell wall, confirming that no substantial pectin hydrolysis is observed. Both images have the same intensity scale. Plants were treated the same way as these presented in Fig. 4 and described in the Materials and Methods. The tissue during the immunolabeling were position side by side on the same slide. LM19 antibody was used to label low-methylesterified HG.

Movie S1

Video showing the localization of the LM20 epitope tagged with Alexa647 (orange-violet colormap encodes the Z-position in the range 0-750 nm) and 2F4 tagged with CF568 (green) in the lobe of the anticlinal wall of Arabidopsis WT cotyledon. The data shown are the same as in Fig. 1C.

Movie S2

Video showing the localization of LM20 antibody tagged with CF568, (orange-violet colormap encodes the Z-position in the range 0-750 nm). Staining includes a junctional part of an anticlinal wall, which gradually slopes down and flattens to create a horizontal wall. The data shown are the same as in Fig. 1E.

Movie S3

Video showing the localization of the 2F4 antibody tagged with Alexa647 (orange-violet colormap encodes Z-position in the range 0-750 nm). Staining includes a junctional part of an anticlinal wall which gradually slopes down and flattens to create a horizontal wall. The data shown are the same as in Fig. 1E.

Movie S4

Video showing the localization of LM20 antibody tagged with CF568 (green) and 2F4 antibody tagged with Alexa647 (orange-violet colormap encodes the Z-position in the range 0-750 nm). Staining includes a junctional part of an anticlinal wall, which gradually slopes down and flattens to create a horizontal wall. Here, as compared to Movies 1 and 2, the data were filtered using 3D Voronoi diagrams to enhance the densest localization, which helps to view the curved 3D structure of the junction between anticlinal and periclinal walls. The data shown are the same as in Fig. 1E.

Movie S5

Video showing the localization of the 2F4 antibody tagged with Alexa647 (orange-violet colormap encodes the Z-position in the range 0-750 nm) in the lobe of the anticlinal wall of Arabidopsis WT cotyledon. The data shown are the same as in Fig. S5D.

Movie S6

Video showing the localization of the LM20 antibody tagged with CF568 (orange-violet colormap encodes the Z-position in the range 0-750 nm) in the lobe of the anticlinal wall of Arabidopsis WT cotyledon. The data shown are the same as in Fig. S5D.

Movie S7

Time-lapse movie acquired with a Keyence digital microscope showing the epidermis of a WS cotyledon before, during, and after dehydration. During dehydration, the loss of turgor did not influence the anticlinal wall shape of the pavement cells. Dehydration did lead to loss of tension in the periclinal walls, which can be seen as an increase in the white regions, the regions perpendicular to the coaxial light, and in the wrinkling of the walls. The change in the shape of periclinal walls was more pronounced in the concave part of the lobe (white) as compared to the convex part, which remained green. The data shown are the same as in Fig. 4B.

Audio S1

The data sonification of cellular shape (the same cell as in Fig. S1, B and C). Cellular contours were resampled so that each day (days 1, 2, 3), they count the same number of points. This assures that there is no change in the pitch due to cell growth, but only due to the enrichment of cellular spectra (appearance of new overtones in the Fourier Transform) due to the formation of new lobes. In this audio file, three days are played successively and can be heard as an increase in pitch, representing new lobe formation with shorter wavelengths. The amplitude increase in the existing lobe is perceived as the volume increase for a given frequency.

Audio S2

The data sonification of cellular shape from the PME13oe cotyledon. The pitch difference between three consecutive days is less apparent (compared to Audio File S1), as almost no new lobes are formed and therefore fewer new overtones are heard.

References

1. O. Hamant, M. G. Heisler, H. Jönsson, P. Krupinski, M. Uyttewaal, P. Bokov, F. Corson, P. Sahlin, A. Boudaoud, E. M. Meyerowitz, Y. Couder, J. Traas, Developmental patterning by mechanical signals in Arabidopsis. *Science* **322**, 1650–1655 (2008).
2. A. Peaucelle, R. Wightman, H. Höfte, The Control of Growth Symmetry Breaking in the Arabidopsis Hypocotyl. *Curr. Biol.* **25**, 1746–1752 (2015).
3. M. Bosch, A. Y. Cheung, P. K. Hepler, Pectin methylesterase, a regulator of pollen tube growth. *Plant Physiol.* **138**, 1334–1346 (2005).
4. F. Nicol, I. His, A. Jauneau, S. Vernhettes, H. Canut, H. Höfte, A plasma membrane-bound putative endo-1,4- β -D-glucanase is required for normal wall assembly and cell elongation in Arabidopsis. *EMBO J.* **17**, 5563–5576 (1998).
5. A. Bichet, T. Desnos, S. Turner, O. Grandjean, H. Höfte, BOTERO1 is required for normal orientation of cortical microtubules and anisotropic cell expansion in Arabidopsis. *Plant J.* **25**, 137–148 (2001).
6. T. Zhang, Di. Vavylonis, D. M. Durachko, D. J. Cosgrove, Nanoscale movements of cellulose microfibrils in primary cell walls. *Nat. Plants.* **3**, 17056 (2017).
7. A. R. Paredez, C. R. Somerville, D. W. Ehrhardt, Visualization of cellulose synthase demonstrates functional association with microtubules. *Science* **312**, 1491–1495 (2006).
8. L. Tan, S. Eberhard, S. Pattathil, C. Warder, J. Glushka, C. Yuan, Z. Hao, X. Zhu, U. Avci, J. S. Miller, D. Baldwin, C. Pham, R. Orlando, A. Darvill, M. G. Hahn, M. J. Kieliszewski, D. Mohnen, An Arabidopsis cell wall proteoglycan consists of

- pectin and arabinoxylan covalently linked to an arabinogalactan protein. *Plant Cell*. **25**, 270–287 (2013).
9. M. A. Atmodjo, Z. Hao, D. Mohnen, Evolving Views of Pectin Biosynthesis. *Annu. Rev. Plant Biol.* **64**, 747–779 (2013).
 10. T. Wang, M. Hong, Solid-state NMR investigations of cellulose structure and interactions with matrix polysaccharides in plant primary cell walls. *J. Exp. Bot.* **67**, 503–514 (2015).
 11. A. Peaucelle, *Cell wall expansion: Case study of a biomechanical process* (Springer, Cham, 2018; http://link.springer.com/10.1007/978-3-319-69944-8_7), vol. 23.
 12. D. J. Cosgrove, Plant cell wall extensibility: Connecting plant cell growth with cell wall structure, mechanics, and the action of wall-modifying enzymes. *J. Exp. Bot.* **67**, 463–476 (2016).
 13. T. I. Baskin, ANISOTROPIC EXPANSION OF THE PLANT CELL WALL. *Annu. Rev. Cell Dev. Biol.* **21**, 203–222 (2005).
 14. A. M. D. Wiedemeier, J. E. Judy-March, C. H. Hocart, G. O. Wasteneys, R. E. Williamson, T. I. Baskin, Mutant alleles of Arabidopsis RADIALLY SWOLLEN 4 and 7 reduce growth anisotropy without altering the transverse orientation of cortical microtubules or cellulose microfibrils. *Development*. **129**, 4821–4830 (2002).
 15. Y. Fu, T. Xu, L. Zhu, M. Wen, Z. Yang, A ROP GTPase Signaling Pathway Controls Cortical Microtubule Ordering and Cell Expansion in Arabidopsis. *Curr. Biol.* **19**, 1827–1832 (2009).

16. A. Sapala, A. Runions, R. S. Smith, Mechanics, geometry and genetics of epidermal cell shape regulation: different pieces of the same puzzle. *Curr. Opin. Plant Biol.* **47**, 1–8 (2019).
17. M. Majda, P. Grones, I. M. Sintorn, T. Vain, P. Milani, P. Krupinski, B. Zagórska-Marek, C. Viotti, H. Jönsson, E. J. Mellerowicz, O. Hamant, S. Robert, Mechanochemical Polarization of Contiguous Cell Walls Shapes Plant Pavement Cells. *Dev. Cell.* **43**, 290-304.e4 (2017).
18. B. Altartouri, A. J. Bidhendi, T. Tani, J. Suzuki, C. Conrad, Y. Chebli, N. Liu, C. Karunakaran, G. Scarcelli, A. Geitmann, Pectin Chemistry and Cellulose Crystallinity Govern Pavement Cell Morphogenesis in a Multi-Step Mechanism. *Plant Physiol.* **181**, 127–141 (2019).
19. M. D. Walkinshaw, S. Arnott, Conformations and interactions of pectins. II. Models for junction zones in pectinic acid and calcium pectate gels. *J. Mol. Biol.* **153**, 1075–1085 (1981).
20. M. D. Walkinshaw, S. Arnott, Conformations and interactions of pectins. I. X-ray diffraction analyses of sodium pectate in neutral and acidified forms. *J. Mol. Biol.* **153**, 1055–1073 (1981).
21. B. Huang, W. Wang, M. Bates, X. Zhuang, Three-dimensional super-resolution imaging by stochastic optical reconstruction microscopy. *Science* **319**, 810–813 (2008).
22. E. Betzig, G. H. Patterson, R. Sougrat, O. W. Lindwasser, S. Olenych, J. S. Bonifacino, M. W. Davidson, J. Lippincott-Schwartz, H. F. Hess, Imaging intracellular fluorescent proteins at nanometer resolution. *Science* **313**, 1642–1645

- (2006).
23. M. J. Rust, M. Bates, X. Zhuang, Sub-diffraction-limit imaging by stochastic optical reconstruction microscopy (STORM). *Nat. Methods.* **3**, 793–796 (2006).
 24. M. Bates, B. Huang, G. T. Dempsey, X. Zhuang, Multicolor super-resolution imaging with photo-switchable fluorescent probes. *Science* **317**, 1749–1753 (2007).
 25. M. Heilemann, S. van de Linde, M. Schüttpelz, R. Kasper, B. Seefeldt, A. Mukherjee, P. Tinnefeld, M. Sauer, Subdiffraction-Resolution Fluorescence Imaging with Conventional Fluorescent Probes. *Angew. Chemie Int. Ed.* **47**, 6172–6176 (2008).
 26. Y. Verhertbruggen, S. E. Marcus, A. Haeger, J. J. Ordaz-Ortiz, J. P. Knox, An extended set of monoclonal antibodies to pectic homogalacturonan. *Carbohydr. Res.* **344**, 1858–1862 (2009).
 27. F. Liners, J.-J. Letesson, C. Didembourg, P. Van Cutsem, Monoclonal Antibodies against Pectin. *Plant Physiol.* **91**, 1419–1424 (1989).
 28. G. T. Dempsey, J. C. Vaughan, K. H. Chen, M. Bates, X. Zhuang, Evaluation of fluorophores for optimal performance in localization-based super-resolution imaging. *Nat. Methods.* **8**, 1027–1040 (2011).
 29. A. Peaucelle, S. A. Braybrook, L. Le Guillou, E. Bron, C. Kuhlemeier, H. Höfte, Pectin-induced changes in cell wall mechanics underlie organ initiation in Arabidopsis. *Curr. Biol.* **21**, 1720–1726 (2011).
 30. Y. Rui, Y. Chen, H. Yi, T. Purzycki, V. M. Puri, C. T. Anderson, Synergistic pectin degradation and guard cell pressurization underlie stomatal pore formation.

- Plant Physiol.* **180**, 66–77 (2019).
31. N. Kim, *NAFEMS Introduction to Nonlinear Finite Element Analysis* (2014).
 32. E. K. Rodriguez, A. Hoger, A. D. McCulloch, Stress-dependent finite growth in soft elastic tissues. *J. Biomech.* **27**, 455–467 (1994).
 33. A. Sampathkumar, P. Krupinski, R. Wightman, P. Milani, A. Berquand, A. Boudaoud, O. Hamant, H. Jönsson, E. M. Meyerowitz, Subcellular and supracellular mechanical stress prescribes cytoskeleton behavior in Arabidopsis cotyledon pavement cells. *Elife.* **3** (2014), doi:10.7554/eLife.01967.
 34. P. Sotiriou, E. Giannoutsou, E. Panteris, B. Galatis, P. Apostolakos, Local differentiation of cell wall matrix polysaccharides in sinuous pavement cells: its possible involvement in the flexibility of cell shape. *Plant Biol.* **20**, 223–237 (2018).
 35. Z. A. Popper, G. Michel, C. Hervé, D. S. Domozych, W. G. T. Willats, M. G. Tuohy, B. Kloareg, D. B. Stengel, Evolution and Diversity of Plant Cell Walls: From Algae to Flowering Plants. *Annu. Rev. Plant Biol.* **62**, 567–590 (2011).
 36. E. Ficko-Blean, C. Hervé, G. Michel, Sweet and sour sugars from the sea: the biosynthesis and remodeling of sulfated cell wall polysaccharides from marine macroalgae. *Perspect. Phycol.* **2**, 51–64 (2015).
 37. M. Terauchi, C. Nagasato, A. Inoue, T. Ito, T. Motomura, Distribution of alginate and cellulose and regulatory role of calcium in the cell wall of the brown alga *Ectocarpus siliculosus* (Ectocarpales, Phaeophyceae). *Planta.* **244** (2016), doi:10.1007/s00425-016-2516-4.
 38. K. T. Haas, A. Peaucelle, Pectin homogalacturonan nanofilament expansion drives

morphogenesis in plant epidermal cells, v1, Mendeley Data (2020);

<http://doi.org/10.17632/xb3f5jrbwv.1>.

39. K. T. Haas, Grafeo V2 (Version V2.1.0). Zenodo.

<http://doi.org/10.5281/zenodo.3663608>.

40. K. T. Haas, SEMfilaments V1 (Version V.1). Zenodo.

<http://doi.org/10.5281/zenodo.3581097>

41. K. T. Haas, & A. Peaucelle. Shape Spectra Analysis (Version V1.1.0). Zenodo.

<http://doi.org/10.5281/zenodo.3665413>.

42. K. T. Haas, The expanding beam model V1.1.0 (Version V1.1.0). Zenodo.

<http://doi.org/10.5281/zenodo.3664101>.

43. R. Wightman, S. Wallis, P. Aston, Hydathode pit development in the alpine plant *Saxifraga cochlearis*. *Flora*. **233**, 99–108 (2017).

44. K. T. Haas, M. Lee, A. Esposito, A. R. Venkitaraman, Single-molecule localization microscopy reveals molecular transactions during RAD51 filament assembly at cellular DNA damage sites. *Nucleic Acids Res.* **46**, 2398–2416 (2018).